Energy conversion mechanism revealed by ATP-free and ATP-dependent walking of myosin V motor

Noriyuki Kodera[1], Holger Flechsig[1], Takayuki Uchihashi[2], and Toshio Ando[1*]

[1]Nano Life Science Institute, Kanazawa University, Kakuma-machi, Kanazawa 920-192, Japan

[2]Department of Physics, Nagoya University, Chikusa-ku, Nagoya 464-8602, Japan

Abstract

The mechanical processes of ATPase protein motors are coupled to their ATPase reactions. The free energy released at a given step(s) of the ATPase cycle is converted into mechanical work. Therefore, it has long been thought that ATP is the energy source for mechanical work. Here, we show that the double-headed myosin V (M5) motor can perform ATP-free walking. In the presence of ADP, M5 bound to F-actin by both heads makes a forward step when the trailing head is detached by an external force. This forward step harnesses the strain energy in the leading (L) head, provided from the strong binding energy between the L-head and actin. Consequently, strain generation reduces the binding affinity, which manifests as sporadic, brief L-head detachment. Strain generation and brief L-head detachment also occur during ATP-dependent walking to similar extents as during ATP-free walking. These results suggest that the strong binding energy is also converted into mechanical work during ATP-dependent walking.

ATP has been described as the energy source of all living cells. Indeed, ATPase motor proteins, including myosin, kinesin, dynein and F_1, generate unidirectional force and movement by hydrolysing ATP, thereby performing a variety of cellular functions[1–5]. The mechanical work is performed by a powerstroke[6,7], which is defined as a rapid structural change that produces a large-scale motion comparable to the molecular size or as the formation of a highly strained conformation[8]. In the latter case, large-scale motion is generated by relaxation of the strain[8].

This article examines the energy conversion mechanism in myosin V (M5), a double-headed processive motor protein that moves by hand-over-hand walking toward the plus end of F-actin with ~36 nm advance per ATP hydrolysis cycle[9-13]. The term 'head' is defined as the motor domain plus the neck domain, while the term 'lever-arm' represents the neck domain plus the neck−motor domain junction (alias the converter hinge). Figure 1 illustrates a generally accepted chemomechanical cycle in M5 with a truncated tail (M5-HMM). M5-HMM will be referred to simply as M5. The cycle starts from the double-headed bound (DHB) state, where the trailing (T) head is nucleotide-free (NF) and the leading (L) head is bound to ADP. The neck domains of the T and L heads are oriented in forward and backward directions, respectively. However, the direction of the L-head neck region near the motor domain is often biased toward the forward direction, causing the entire neck to bend outward. This bending was observed by negative stain electron microscopy (nsEM) at low concentrations (0.5–1.0 μM) of ATP[14]. At such low concentrations of ATP, ATP binding to the T-head is the primary rate-limiting step[15,16], and therefore, M5 is predominantly in the initial state of the chemomechanical cycle (Fig. 1, top). ADP bound to the L-head is virtually unable to dissociate due to the strained structure of the L-head, which is the basis for processive hand-over-hand walking[13,17,18].

The chemomechanical cycle progresses as follows (Fig. 1). (1) Upon binding to ATP, the T-head detaches via a structurally revealed mechanism[19], resulting in a forward swing of the L-head lever-arm through its strain relaxation. (2) The ATP bound to the detached head is rapidly

hydrolysed into ADP and inorganic phosphate (Pi), resulting in a change in the angle between the motor and neck domains by 80–90°[20-22] via a structurally revealed mechanism[21,22]. This change in angle is known as the recovery stroke. It directs the actin-binding site of the motor domain to a forward actin site, thereby promoting head binding to actin in a backward-tilt orientation. (3) The detached head, undergoing Brownian motion around the forward-shifted neck−neck junction that is also undergoing Brownian motion, searches for a forward actin site. (4) Upon actual binding to an actin site weakly, the bound head becomes the new L-head in a primed pre-powestroke conformation. The structure of this transient primed state has recently been elucidated by time-resolved cryo-EM[23]. The step size, or the separation between the two motor domains bound to F-actin, which we refer to as the 'motor domain (MD) separation', is approximately $36 \pm n \times 5.5$ nm, where $n = -2, -1, 0, 1, 2, 3, 4$ for phalloidin-free F-actin, and $n = -1, 0, 1, 2$ for phalloidin-stabilised F-actin[24]. The number of actin subunits contained within the MD-separation is $N_{\text{m-m}} = 13 \pm 2n$. This discrete variation in actin sites available for head binding is the consequence of two factors: the nearly straight walking of M5 on F-actin with minimal azimuthal distortion in the DHB state[25] and the temporal variation in the F-actin helical pitch due to cumulative angular disorder between adjacent actin subunits[24]. (5) Pi is released from the new L-head, which strengthens the L-head–actin binding. This strong binding leads to the generation of a powerstroke, which is associated with a bend-to-straight conformational change in the L-head[26,27]. However, the order of Pi release and force generation in any myosin class is currently under debate[28–34]. Nevertheless, the crystal structure of myosin VI[29] containing Pi in its putative escape route (termed 'the backdoor tunnel'[35]) suggests that the force generation occurs when Pi has left from the active site yet remains at the tunnel exit[29,36]. We follow this structurally suggested scenario, since the weak binding between actin and M5 with ADP·Pi at the active site would hinder the generation of a strong force[36]. (6) ADP is released from the T head, resulting in an additional forward shift of the neck–neck junction

73 by 2–6 nm[17,37] and the restoration of the M5 molecule to its initial state (but with an advance by
74 36 ± n × 5.5 nm).

75 In the initial state (Fig. 1, top), the L-head is mainly strained through Pi release, which is
76 reflected in its bending. This strain is used for the L-head swing after T-head detachment. However,
77 nsEM[14] and high-speed atomic force microscopy (HS-AFM)[38] have also observed L-head bending
78 in the presence of ADP. HS-AFM has additionally detected occasional unfolding of the short coiled-
79 coil tail of M5 in the DHB state, resulting in M5 monomerisation[38]. This unfolding was not caused
80 by the AFM tip, as monomerised M5 was also observed in nsEM images of M5 purified by co-
81 pelleting with F-actin[39]. Following tail unfolding, the monomerised L-head rotated forward in a
82 manner similar to the swinging lever-arm motion observed in the presence of ATP[38]. Therefore, in
83 the presence of ADP, the DHB M5 may potentially step forward when its T-head is mechanically
84 detached, rather than by ATP binding. In the present study, we examined this possibility by using
85 interactive HS-AFM (iHS-AFM), where the AFM tip was used for both molecular imaging and head
86 detachment. Based on these and other observations, we investigated the energy conversion
87 mechanism in ATP-dependent walking of M5.

88 Results

89 ATP-free walking of M5

90 In the present study, we used M5 from chick brain[40,41]. The assay system used for HS-AFM
91 observation of M5 interacting with phalloidin-labelled F-actin immobilised on a lipid bilayer surface
92 is identical to that employed previously[38] (Fig. 2a and Methods). The lipid bilayer also contains 5%
93 (w/w) of a positively charged lipid that weakly attracts M5 molecules to the bilayer surface. This
94 attraction provides M5 molecules with a mechanical load against their movement along F-actin.
95 This load reduces the translocation velocity by 27% at saturating concentrations of ATP[38].

96 In the presence of 1 mM ADP, M5 molecules were bound to F-actin by both heads with $N_{m\text{-}m}$ =
97 11 (1.5%), 13 (90.7%), 15 (7.6%), and 17 (0%) actin subunits (typical AFM images are shown in
98 Fig. 2b, top). M5 molecules with $N_{m\text{-}m}$ = 2 also appeared by 0.12%, where the two heads were
99 bound to adjacent actin subunits within the same single strand of double-stranded F-actin. Even
100 in the presence of 0.1 and 1 μM ATP, this type of binding occurred to a similar extent as in the
101 case of ADP. Its typical AFM image is shown in Fig. 2b, bottom, together with an AFM image of
102 M5 with $N_{m\text{-}m}$ = 13 that appeared before forming $N_{m\text{-}m}$ = 2 at 1 μM ATP. For molecules with $N_{m\text{-}m}$ =
103 2, we did not perform any additional experiment and analysis. The dynamic process leading to the
104 DHB state could not be captured with HS-AFM, as this binding had already been completed by
105 the time the HS-AFM system was ready for imaging after the addition of M5. Nonetheless, the
106 observation of double-headed binding with $N_{m\text{-}m}$ = 11, 13, and 15 suggests that the unbound head,
107 which is destined to become the L-head, must have undergone a thermally induced angle change
108 at the converter hinge prior to reaching the final state. Otherwise, the unbound head would have
109 been unable to bind actin in the backward-tilt orientation. Although it is uncertain whether this
110 angle change is similar to the structurally defined recovery stroke[21,22], we refer to this thermally
111 induced angle change as a thermal recovery stroke. Unexpectedly from the crystal structures of
112 M5, previous nsEM observations of M5 alone revealed a NF head that was largely bent by ~90˚
113 at the neck–motor domain junction (resembling a post-recovery stroke conformation) as well as a
114 straighter head at 100 μM ATP (resembling a post-powerstroke conformation)[42]. The appearance
115 frequencies of these conformations were lower than those of opposite counterparts under the
116 respective conditions[42]. Therefore, the neck–motor domain junction is sufficiently flexible to permit
117 a thermal recovery stroke to occur in the presence of ADP. However, upon binding to actin, the
118 converter hinge angle that has been temporarily altered by a thermal recovery stroke rapidly
119 redistributes itself around the most stable angle, which is restricted by the strong head–actin
120 binding. It can thus be inferred that L-head binding to actin following a thermal recovery stroke

121 results in the L-head being subjected to strain. To ascertain whether ADP-bound M5 can advance
122 by harnessing the strain energy acquired presumably in this way, we employed the iHS-AFM
123 technique[43,44], as explained below.

124 For the HS-AFM imaging of actin-bound M5 in the presence of 1 mM ADP, 0.1 μM ATP, or 1
125 μM ATP, the cantilever oscillation amplitude to be maintained during imaging (i.e., the set-point
126 amplitude A_s) was set to 0.9 × A_0, where A_0 (= 1.5 nm) is the free oscillation amplitude. Therefore,
127 the mean oscillation energy loss per tip–sample contact, ΔE_{ts}, was estimated to be ΔE_{ts} = 3.1–4.7
128 $k_B T$ (k_B, Boltzmann constant; T = 298 in kelvin) from the mechanical properties of the short
129 cantilevers used (see Methods). In iHS-AFM (Supplementary Fig. 1), which is used only in the
130 presence of 1 mM ADP, the operator of the HS-AFM system specifies a pixel position within the
131 successively displayed molecular images using a PC mouse pointer and then pushes a start key
132 to initiate the interactive mode in the next frame of imaging. It should be noted that the T- and L-
133 heads can be readily distinguished from one another. This is based on the curved L-head and also
134 on a specific rule between the polarity of F-actin and the direction in which the heads bind to actin[45]
135 (Supplementary Fig. 2).

136 When the cantilever tip reaches a locus within a molecule corresponding to the specified pixel,
137 A_s is rapidly reduced to a preset level A_p. This results in the application of a controlled strong force
138 to the specified locus by moving the sample stage vertically towards the oscillating tip. Immediately
139 after this large force application, the system returns to the normal imaging mode. The HS-AFM
140 system interprets this excessive vertical displacement as a very low height of the locus, such that
141 the specified pixel appears darker in the image. In the experiments described below, A_p was set
142 to 0.33 × A_0 (= 0.5 nm), corresponding to ΔE_{ts} = 14.6–22.0 $k_B T$. Furthermore, to ensure 100%
143 head detachment, the strong force was applied to closely positioned 7 × 7–11 × 11-pixel points
144 including the operator-specified point at their centre (for more details, see Supplementary Fig. 1).
145 It should be noted that the oscillation energy, ΔE_{ts} = 3.1–4.7 $k_B T$ or 14.6–22.0 $k_B T$, is transferred

146 to the sample at each tip–sample contact. However, this transferred energy dissipates rapidly
147 (within much shorter than the oscillation period of ~1 μs) into the surrounding water. Consequently,
148 the transferred energy does not accumulate in the sample, as demonstrated by the HS-AFM
149 imaging of the stator ring of F_1-ATPase at 12.5 fps for 40 s using a cantilever with a resonant
150 frequency of 1.2 MHz in water, where repeated conformational changes were continuously
151 observed without any loss of activity[46]. In these conditions, a single stator ring was iteratively
152 tapped with the tip tens of millions of times.

153 The application of a strong force to a motor domain (Fig. 2c) could detach the motor domain
154 from actin with nearly 100% probability. The event of no detachment only rarely occurred but
155 tended to occur when the motor domain shifted its position due to a change of the F-actin helical
156 pitch that occurred by chance just prior to the initiation of the interactive mode. Since the vertically
157 applied strong force pushes the motor domain toward its bound actin subunit, head detachment
158 is very likely to be caused by brief structural deformation of the motor domain. When a strong
159 force was applied to the L-head motor domain, the molecule appeared to remain in the same
160 position despite brief detachment of the L-head. This detachment was confirmed by the brief
161 disappearance of the motor domain from the image (Supplementary Fig. 3). In contrast, when the
162 T-head motor domain was detached by the strong force, the molecule stepped forward with a high
163 probability (92.5%). When this operation was repeated, the molecule almost always advanced in
164 each interactive-mode operation, resulting in a long-range movement (Fig. 2d; Supplementary
165 Video 1). It is noteworthy that the stepping direction was independent of the scanning direction
166 (Supplementary Fig.4; Supplementary Video 2). Therefore, the observed forward stepping is not
167 attributed to tip dragging. Furthermore, M5 retained its ATP-dependent motor activity after
168 repeated application of a strong force, as evidenced by processive walking of such molecules after
169 the addition of ATP by the UV photolysis of caged-ATP (Supplementary Fig. 5; Supplementary
170 Video 3).

171 **Comparison of strain energies in different nucleotide conditions and MD-separations**

172 The observed ATP-free walking indicates that the forward step of M5 uses the strain energy in the
173 L-head provided just by the double-headed binding to F-actin. A crucial question is whether the
174 mechanism of energy usage in ATP-dependent walking is identical to that in ATP-free walking. It
175 remains unclear whether the strained L-head in the DHB state formed via the ADP·Pi-induced
176 recovery stroke and subsequent Pi release is identical (or similar) to that formed via the thermal
177 recovery stroke alone. To address this question, a quantitative comparison of the strain energies
178 produced in the three nucleotide conditions (1 mM ADP, 0.1 μM ATP, or 1 μM ATP) was made. It
179 is important to note that the chemical state of the T-head depends on the nucleotide conditions. In
180 the presence of 0.1 and 1 μM ATP, the actin-bound T-head is predominantly NF, judging from the
181 ADP dissociation rate constant of 7.2 s^{-1} at the T-head under the experimental conditions[38],
182 whereas the L-head is bound to ADP in all three conditions.

183 In the DHB state, M5 is primarily subjected to strain at the converter hinges of the T and L
184 heads, as well as at the neck domain of the L-head. To estimate the strain energy at each site, the
185 distribution of the neck orientation angle (φ), relative to the F-actin orientation, of single-headed
186 M5 bound to F-actin was first measured for both ADP-bound and NF states[38] (Fig. 3a). The angular
187 spring constants of the converter hinge $K(\varphi)$, as estimated from the respective angle distributions
188 $P(\varphi)$, are dependent on the angle. For instance, at 1 mM ADP, the spring constant K_{ADP} is 23.0
189 $k_BT\cdot rad^{-2}$ at the equilibrium angle φ_0 = 28.5˚, decreasing with increasing φ (Fig. 3b, solid red line).
190 In the NF state, the angular spring is stiffer. For instance, the spring constant K_{NF} is 40.0 $k_BT\cdot rad^{-}$
191 ^{2} at φ_0 = 28.5˚ and 37.9 $k_BT\cdot rad^{-2}$ at the equilibrium angle in the NF state, φ_0 = 32.9˚ (Fig. 3b,
192 dashed red line). The potential energies of the converter hinge in the ADP-bound and NF states,
193 $U_D(\varphi)$ and $U_{NF}(\varphi)$, are shown in Fig. 3b with the black solid and black dashed lines, respectively.
194 The corresponding forces $F(\varphi)$ generated, in parallel to F-actin, at the neck free end in the ADP-
195 bound and NF states are shown in Fig. 3b with the blue solid and blue dashed lines, respectively.

196 $F(\varphi)$ in the ADP-bound state approaches a plateau (approximately 2.2 pN) at $\varphi > 100^\circ$, which is
197 consistent with the reported stall force for M5, 1.9–3.0 pN[47-49]. The derivation of these mechanical
198 quantities is described in Methods.

199 Subsequently, the geometric parameters of M5 in the DHB state were measured: the tangential
200 angle of the L-head neck region emerging from the motor domain, φ_L, the angle of the T-head
201 neck as a function of φ_L, $\varphi_T(\varphi_L)$, and the deflection of the L-head neck end (at the neck−neck joint)
202 as a function of φ_L, $h(\varphi_L)$ (see Fig. 3c, inset). The experimental data of $h = h(\varphi_L)$ and $\varphi_T = \varphi_T(\varphi_L)$
203 were fitted to the fourth and second polynomial functions, respectively (solid lines in Fig. 3c,d for
204 $N_{m\text{-}m}$ = 13 actin subunits and in Supplementary Fig. 6a-d for $N_{m\text{-}m}$ = 11 and 15 actin subunits). Note
205 that each solid line is drawn in a range of observed angles of φ_L. The maximum angle of φ_L
206 (denoted with φ_L^{max}), where the L-head neck deflection was extrapolated to zero, was
207 approximately 127° for $N_{m\text{-}m}$ = 11, 135° for $N_{m\text{-}m}$ = 13, and 145° for $N_{m\text{-}m}$ = 15, irrespective of the
208 nucleotide conditions. For each MD-separation, the fitted curves for $h = h(\varphi_L)$ are nearly identical
209 across the three nucleotide conditions (the three solid lines in Fig. 3c for $N_{m\text{-}m}$ = 13 and those in
210 Supplementary Fig. 6a,b for $N_{m\text{-}m}$ = 11 and 15). This is also the case for $\varphi_T = \varphi_T(\varphi_L)$ (the three
211 solid lines in Fig. 3d for $N_{m\text{-}m}$ = 13 and those in Supplementary Fig. 6c,d for $N_{m\text{-}m}$ = 11 and 15). The
212 only distinct difference between the nucleotide conditions is that the minimum value of φ_L that the
213 L-head can take is smaller (approximately by 20−30°) in the presence of ATP than in the presence
214 of ADP (see the left end of each fitted solid lines in Fig. 3c,d and Supplementary Fig. 6a−d). Since
215 φ_T is always larger than the equilibrium angles φ_0 of single-headed M5 (28.5° for the ADP-bound
216 head, and 32.9° for the NF-head) irrespective of the nucleotide conditions, the stiffer NF T-head
217 at 0.1 and 1 μM ATP pushes the ADP-bound L-head at the neck-neck junction more strongly than
218 the less stiff ADP-bound T-head at 1 mM ADP (Fig. 3d, inset), resulting in the smaller minimum
219 value of φ_L in the presence of ATP. This is how the 2-6 nm forward shift of the neck−neck (or
220 neck−tail) junction occurs when ADP detaches from the T-head[17,37].

The DHB state remains stationary under all nucleotide conditions, except for thermal fluctuations. Consequently, all forces acting on a M5 molecule in the DHB state, including the constraining forces, are balanced. As such, the sum of the strain energies at the three sites is conserved (from the principle of virtual work in mechanics; see Methods). When the strain energies at the converter hinges of the T and L heads and at the neck domain of the L-head are denoted as U_{TCH}, U_{LCH}, and U_{neck}, respectively, the sum $U_{TCH}[\varphi_T(\varphi_L)] + U_{LCH}(\varphi_L) + U_{neck}[h(\varphi_L)]$ is constant ($\equiv E_{total}$) over possible values of φ_L, under a given condition. The value of $U_{TCH}[\varphi_T(\varphi_L)]$ can be estimated from $U_D(\varphi)$ or $U_{NF}(\varphi)$ at $\varphi = \varphi_L$ (solid or dashed black lines in Fig. 3b) depending on the nucleotide condition, while the value of $U_{LCH}(\varphi_L)$ can be estimated from $U_D(\varphi)$ at $\varphi = \varphi_L$ (solid black line in Fig. 3b). The resulting $U_{TCH}[\varphi_T(\varphi_L)]$ and $U_{LCH}(\varphi_L)$ for $N_{m\text{-}m} = 13$ are shown in Fig. 3e with the dotted lines and the black solid line (common to all nucleotide conditions, except for the angle ranges), respectively, and those for $N_{m\text{-}m} = 11$ and 15 are shown in Supplementary Fig. 6e,f. The value of E_{total} can be obtained as $E_{total} = U_{TCH}[\varphi_T(\varphi_L^{max})] + U_{LCH}(\varphi_L^{max})$. The results are shown in Fig. 3e with solid horizontal lines for $N_{m\text{-}m} = 13$, while those for $N_{m\text{-}m} = 11$ and 15 are shown in Supplementary Fig. 6e,f. As can be clearly seen by the solid horizontal lines in these figures, the total strain energy is very similar (around ~10 k_BT) across the three nucleotide conditions. It is also similar across the different MD-separations. This similarity across the different MD-separations is consistent with the report that there is no significant difference in the kinetics of ATP-dependent walking regardless of the stride length[24]. The strain energy used for the mechanical work performed by the L-head swing after T-head detachment is not the total strain energy E_{total} but $U_{LCH}(\varphi_L) + U_{neck}[h(\varphi L)]$ (dashed lines located just below the solid horizontal lines in Fig. 3e and Supplementary Fig. 6e,f). However, the contribution of $U_{TCH}[\varphi_T(\varphi_L)]$ to E_{total} is small and almost identical across the three nucleotide conditions, although the maximum value of $U_{TCH}[\varphi_T(\varphi_L)]$ differs across the different MD-separations (0.5 k_BT for $N_{m\text{-}m} = 15$, 0.7 k_BT for $N_{m\text{-}m} = 13$, and 1.5 k_BT for $N_{m\text{-}m} = 11$). Thus, the strain energy to be used for the forward step is very

246 similar between ATP-free walking and ATP-dependent walking, despite the different pathways to
247 the strained state as described above.

248 The value of $U_{neck}[h(\varphi_L)]$ can be obtained as $U_{neck}[h(\varphi_L)] = E_{total} - U_{TCH}[\varphi_T(\varphi_L)] - U_{LCH}(\varphi_L)$ (long
249 dashed lines in Fig. 3e and Supplementary 6e,f). The spring constant of the L-head neck, k_{neck},
250 estimated from $U_{neck}[h(\varphi_L)]$ depends on φ_L and the MD-separation (Fig. 3f and Supplementary Fig.
251 6g,h). These dependencies indicate that larger neck bending (i.e., smaller φ_L) results in smaller
252 k_{neck}. The value of k_{neck} varies around 0.18 pN/nm, a value previously estimated using optical
253 tweezers[17]. Note that the estimated values of the spring constant in the large φ_L regions are not
254 reliable because the values were obtained by dividing the values of $2U_{neck}$ by small values of h^2.

255 **Foot stomping**

256 If a M5 molecule is bound to actin solely by the T-head, the molecule will not undergo strain except
257 for that induced by thermal effects. Therefore, the total strain energy in M5 in the DHB state at 1
258 mM ADP originates from the strong binding energy between the L-head and actin. Interestingly, it
259 was observed at 1 mM ADP that the L-head occasionally detached from actin and then quickly
260 reattached to F-actin at the same position or its vicinity (Supplementary Fig. 7a; Supplementary
261 Video 4). This behaviour, which occurs predominantly at the L-head, was previously observed by
262 HS-AFM also in the presence of 0.1 and 1 μM ATP[38]. This behaviour is referred to as 'foot stomp'.
263 In our previous study, positional shifts of the motor domains approximately by ±5.5 nm without
264 detachment (Supplementary Fig. 7b,c; Supplementary Vide 5) were misclassified also as foot
265 stomp. The positional shifts without detachment are now referred to as ‘foot sliding’ and are
266 understood to result from changes in the helical pitch of F-actin. The foot sliding was observed to
267 occur at either head (L-head, Supplementary Fig. 7b; T-head, Supplementary Fig. 7c), resulting in
268 wider or shorter MD-separations. Foot stomping is not due to tip force, as similar behaviour has
269 been observed during ATP-dependent M5 walking using interferometric scattering (iSCAT)

microscopy[50] and polarised fluorescence microscopy[51]. The frequency of foot stomping observed with iSCAT was ~3% of steps taken at 1 μM ATP, ~0.6% of steps taken at 10 μM ATP, and none at saturating ATP[50]. The lower frequency at higher ATP concentrations is likely attributable to the T-head being detached by its binding to ATP during L-head foot stomping, resulting in complete dissociation of the molecule. Such foot stomp events would have been excluded from the count. This complete dissociation is likely to be one of the mechanisms by which processive walking of M5 is terminated. Since single-headed M5–ADP has a high affinity for actin (K_d = 7.6 × 10^{-9} M, corresponding to a binding energy of –18.7 k_BT)[16], foot stomping at the L-head is most likely caused by a reduction in its binding energy equivalent to the total strain energy of ~10 k_BT. Therefore, the affinity of the L-head reduces to approximately K_d = Exp[(–18.7 + 10)] ≈ 1.7 × 10^{-4} M in the DHB state under the three nucleotide conditions, which must manifest as foot stomping. We verified this issue by estimating the foot stomp rate (R_{stomp}) by counting the number of foot stomp events (N_{stomp}) out of the total number of imaged frames (N_{total}), as $R_{stomp} = N_{stomp}/N_{total}$ × imaging rate, where N_{stomp} observed at different MD-separations were summed. This summation is because the total strain energy is similar between different MD-separations. As shown in Table 1, R_{stomp} was similar across the three nucleotide conditions (0.069 s^{-1}, 0.064 s^{-1}, and 0.109 s^{-1} at 1 mM ADP, 0.1 μM ATP, and 1 μM ATP, respectively). Our results of R_{stomp} are similar to those estimated from the frequencies of foot stomping observed with iSCAT microscopyy[50], although some foot stomp events are likely to be missed at 10 μM ATP due to complete dissociation of M5: 0.05 s^{-1} and 0.04 s^{-1} at 1 μM and 10 μM ATP, respectively. Here, the second-order ATP binding rate constant (2.0 $\mu M^{-1}s^{-1}$) and the ADP dissociation rate constant (10.8 s^{-1})[38] at the T-head were used to estimate R_{stomp} from the foot stomp frequencies observed by iSCAT microscopy[50]. Thus, the generation of molecular strain reduces the affinity of the L-head for actin, resulting in foot stomping, while the generated strain energy $U_{LCH}(\varphi_L) + U_{neck}[h(\varphi_L)]$ is converted into mechanical work performed by the actin-bound L-head during both ATP-free and ATP-dependent walking.

295 **Table 1 | Foot stomp events observed under three nucleotide conditions**

Nucleotide conditions	Total number of images	Number of foot stomp events	Imaging rate (fps)	Foot stomp rate (s^{-1})
1 mM ADP	25,790	588	3.0	0.068
0.1 μM ATP	7,441	71	6.67	0.064
1 μM ATP	5,709	93	6.67	0.109

296

297 Although very rare, M5 exhibited 30 instances of a backward step following spontaneous L-
298 head detachment, among the 25,790 images captured in the presence of 1 mM ADP. To counteract
299 this backward step, M5 displayed 28 forward steps following spontaneous T-head detachment in
300 the presence of 1 mM ADP. The similar frequencies of the forward and backward steps caused by
301 spontaneous head detachment are therefore consistent with the principle of detailed balance
302 under thermal equilibrium.

303 **Energetics of ATP-free and ATP-dependent walking**

304 This section uses an energy landscape to quantitatively explain the relatively low success/failure
305 ratio in ATP-free walking compared to ATP-dependent walking. This landscape leads to the
306 landing of the detached head on F-actin through molecular processes occurring at the detached
307 and attached heads. The results show the ADP·Pi-induced recovery stroke greatly contributes to
308 the high degree of successful forward stepping in ATP-dependent walking, despite a small free
309 energy being expended for the recovery stroke.

310 In ATP-free walking, the T-head, detached from actin by the strong tip force, reaches the next
311 forward binding site through the following stages: (i) thermal recovery stroke by the detached head,
312 (ii) forward swing of the actin-bound L-head, and (iii) Brownian search of the detached head for
313 the next binding site[47,50,52,53.]. The Brownian search is performed by rotational diffusion of the
314 bound head around the equilibrium angle relative to F-actin and by rotational diffusion of the
315 detached head around the neck–neck junction (see Fig. 4a,b). However, the energy spent in the

latter Brownian rotation is negligible[54,55] because the neck–neck joint is highly flexible as indicated by the wide distribution of the angle made by the two necks at the joint[56]. Thus, the following equation holds for the success/failure ratio (= 0.925/0.075) of ATP-free forward stepping:

$$\frac{\text{success}}{\text{failure}} = \left[\frac{\text{thermal recovery stroke}}{\text{without recovery stroke}}\right]_{\text{detached head}} \times \left[\frac{\text{forward swing}}{\text{backward swing}}\right]_{\text{bound head}}. \qquad (1)$$

Here, the denominators and the numerators on the right-hand side represent the probabilities of respective molecular actions. From Eq.(1), the overall energy barrier difference between the forward step and the backward return after T-head detachment (ΔE_0) is equal to the sum of the energy barrier differences corresponding to the first term (ΔE_1) and the second term (ΔE_2) on the right side of Eq.(1), i.e.,

$$\Delta E_0 = \Delta E_1 + \Delta E_2. \qquad (2)$$

In the failure events, the detached motor domain returned to the original actin site or its vicinity. Despite the low probability of backward return, the distribution of MD-separations formed immediately after backward return was similar to that of forward step (pink and red bars in Supplementary Fig. 8). This similarity indicates that the distribution of different MD separations is predominantly determined by the probabilities that the half pitch of F-actin takes approximately 36 ± n × 5.5 nm. Even when the resulting MD separation differs between the two DHB states formed immediately after the success and failure steps, the two states are energetically similar, as the total strain energy (E_{total}) is only slightly sensitive to the MD separation (Fig. 3e and Supplementary Fig. 6e,f). Consequently, the energy landscapes for the forward step and the backward return can be depicted as shown in Fig. 4c, where $G_f^{\ddagger}$ and $G_b^{\ddagger}$ denote the energy barrier heights for the forward step and the backward return, respectively. Their difference is given by $G_f^{\ddagger} - G_b^{\ddagger} = \Delta E_0$.

The overall energy barrier difference ΔE_0 is given by $\Delta E_0 = -k_B T \log_e(\text{success/failure}) = -2.5\ k_B T$ (see Fig. 4c). Next, we estimate the energy barrier difference ΔE_1 between the presence and absence of a thermal recovery stroke by the detached head; see the first term on the right-hand

side of Eq.(1). In ATP-dependent walking, the recovery stroke in the detached head is caused by the ATP hydrolysis into ADP·Pi in the detached head (Fig. 1)[20-22] in a structurally well-defined manner[21,22,57]. The recovery stroke angle $\Delta\varphi_{\mathrm{rs}}$ was previously measured to be 85˚ ± 19˚[20] using a bright-field optical microscope in combination with a UV-flash photolysis system for the release of ATP from caged-ATP. In this measurement, the neck of monomeric M5 was immobilised on a top surface of a bead, while the motion of a double bead specifically attached to the motor domain was observed in real time. The angular spring constant of the neck–motor domain junction in the actin-unbound head was estimated to be k' = 23 pN·nm·rad^{-2} = 5.59 $k_{\mathrm{B}}T$·rad^{-2} from the Gaussian width of the thermally driven angular fluctuations[20], which was very similar between before and after a recovery stroke. The value of the angular spring constant is also similar to that of muscle myosins[58]. It is noteworthy that the spring constant k' is significantly smaller than those of the single-headed M5 bound to actin in the ADP-bound and NF conditions, K_{ADP} and K_{NF}, respectively (Fig. 3b). Thus, actin binding largely stiffens the converter hinge. Supposing that the value of $\Delta\varphi_{\mathrm{rs}}$= 85˚ is the most adequate angle to achieve the MD-separation of 36 nm, $\Delta\varphi_{\mathrm{rs}}$ ranges from 77˚ to 95˚ for covering the MD-separation range of 36 ± 5.5 nm. The mean thermal recovery stroke energy is approximately estimated to be $\Delta E_1 = 0.5 \times k' \times \langle \Delta\varphi_{\mathrm{rs}}{}^2 \rangle = 6.3\ k_{\mathrm{B}}T$, where averaging is made over the angle range of 77˚–95˚. As a consequence of this large uphill process, the forward landing of the detached T-head is slow (approximately 10.7 s^{-1}, corresponding to a characteristic time ≈ 94 ms, Fig. 4d), compared to that observed in ATP-dependent walking (160–180 s^{-1})[47,52]. This result of the landing rate was obtained without considering the different MD-separations formed immediately after landing. For the kinetic scheme of

$$\text{backward return} \xleftarrow{k_{\mathrm{B}}} \text{detached T-head} \xrightarrow{k_{\mathrm{F}}} \text{forward step}$$

with rate constants k_{B} (for backward return) and k_{F} (for forward step), the landing rate k_{landing} should be the same between the two landing processes, i.e. $k_{\mathrm{landing}} = k_{\mathrm{F}} + k_{\mathrm{B}}$; from $k_{\mathrm{F}}/k_{\mathrm{B}}$ = 0.925/0.075,

we obtain k_F = 9.9 s^{-1} and k_B = 0.80 s^{-1}. However, the backward return landing was slower (about 6.0 s^{-1}) than the forward landing, as estimated from the histogram of backward return times (Fig. 4e). This inconsistency is most likely due to the limited number of backward return events, as well as the limited time resolution. The relationship between the forward landing rate and the MD-separation (Fig. 4f,g) will be described later.

From the values $\Delta E_0 = -2.5\ k_BT$ and $\Delta E_1 = 6.3\ k_BT$, the energy barrier difference between the forward and backward swings of the actin-bound head can be indirectly estimated to be ΔE_2 (= $\Delta E_0 - \Delta E_1$) = $-8.8\ k_BT$. However, the value of ΔE_2 can be directly estimated, as described below. Just before forward landing of the detached head, the actin-bound head with ADP makes an angle of 45˚ ± δ relative to F-actin, while just before backward return landing, it makes an angle of 135˚ ± δ, where δ is approximately 10˚, estimated from the differences of φ_L^{max} between different MD-separations. Therefore, ΔE_2 can be estimated as the mean potential energy difference, $\langle U_D(45^\circ)\rangle - \langle U_D(135^\circ)\rangle$, where averaging is made over the angle regions, $45^\circ - \delta \le \varphi \le 45^\circ + \delta$ for $\langle U_D(45^\circ)\rangle$ and $135^\circ - \delta \le \varphi \le 135^\circ + \delta$ for $\langle U_D(135^\circ)\rangle$; see the light-blue regions under the solid black line in Fig. 3b. The values of $\langle U_D(45^\circ)\rangle$ and $\langle U_D(135^\circ)\rangle$ are 0.7 k_BT and 9.4 k_BT, respectively, which yields $\Delta E_2 = -8.7\ k_BT$. This result is in good agreement with the value indirectly estimated above. Thus, the energy landscape derived from Eq.(1) could quantitatively explain the observed success/failure ratio of the forward step in ATP-free walking.

In ATP-dependent walking, failure of the forward step is very rare. This is due to the first term on the right-hand side of Eq. (1) changing to the following form:

$$\left[\frac{\text{ADP}\cdot\text{Pi-induced recovery stroke}}{\text{thermal reversal of recovery stroke}}\right]_{\text{detached head}}. \qquad (3)$$

The second term on the right-hand side of Eq.(1) is common to both ATP-free and ATP-dependent walking. The energy barrier difference ΔE_1 corresponding to the new form (3) becomes $\Delta E_1 = -2.3\ k_BT - (+6.3\ k_BT) = -8.6\ k_BT$. Here, the $-2.3\ k_BT$ is for the ADP·Pi-induced recovery stroke

389 estimated from the ATPase kinetics[16], while 6.3 k_BT is the energy required to thermally reverse the
390 ADP·Pi-induced recovery stroke (i.e., 0.5 × k' × $\langle \Delta\varphi_{rs}{}^2 \rangle$). By including the second term shown in
391 Eq.(1), the overall energy barrier difference between the forward step and the backward return
392 becomes $\Delta E_0 = -8.6\ k_BT - 8.7\ k_BT = -17.3\ k_BT$. The success/failure ratio therefore becomes
393 Exp(–17.3) ≈ 3 × 10^{-8}. The ADP·Pi-induced recovery stroke largely contributes to this high success
394 rate by elevating the energy barrier height for the backward return, despite the small amount of
395 free energy expended (2.3 k_BT).

396 **Mechanical model and simulations of ATP-free M5 translocation**

397 We constructed a simplified mechanical model of the M5 dimer considering converter-hinge
398 energies derived from HS-AFM data for the angular distribution $P(\varphi)$ mentioned above (Methods,
399 Supplementary Information). Brownian dynamics simulations of the model were employed to
400 numerically investigate ATP-free M5 translocation cycles along F-actin (Methods, Supplementary
401 Methods, Supplementary Fig. 9, and Supplementary Table 1). We investigated the following
402 questions: (i) Is the external energy applied with the AFM tip under iHS-AFM scanning sufficient
403 to induce mechanical detachment of the T-head? (ii) How long must the rebinding process for a
404 step in an ATP-free cycle be?

405 As described above, the total strain energy is ~10 k_BT for M5–ADP in the DHB state. To enable
406 binding of an M5 head, the actin-binding energy should at least compensate for this total strain.
407 Thus, the head–actin binding energy is estimated to be at least –10 k_BT. In the ATP-free case, the
408 energy required for mechanically detaching the T-head has to be supplied by the AFM tip, which
409 under interactive mode scanning provides sufficient energy (14.6–22.0 k_BT oscillation energy loss
410 per tap). Importantly, the externally supplied energy is always larger than the amount that is
411 temporarily borrowed from the environment during the thermal recovery stroke (ΔE_1 = 6.3 k_BT for

412 $\Delta\varphi_{rs}$ = 85˚), such that the energy balance for an entire forward step is consistent with the second
413 law of thermodynamics (that is, the energy balance confirms that the steps proceed downhill).
414 Brownian dynamics simulations of the ATP-free M5 stepping revealed a forward landing time
415 of 82 ms (rate, 12.2 s^{-1}; n = 1852), while the backward return landing time was 110.4 ms (rate,
416 9.06 s^{-1}; n = 148). When the loading effect of the substrate surface in the HS-AFM experiment is
417 considered, these values become 112 ms (rate 8.9 s^{-1}) and 151 ms (rate, 6.6 s^{-1}) for the forward
418 and backward return landings, respectively, which are roughly consistent with the HS-AFM data
419 (94 ms for forward landing and 166 ms for backward landing). The step time distribution together
420 with an exemplary time trace of the M5 for consecutive ATP-free stepping and corresponding
421 conformational snapshots of the mechanical M5 model are shown in Supplementary Fig. 10 (also
422 see Supplementary Video 6). Furthermore, the success/failure ratio for a forward step after
423 mechanical T-head detachment obtained from simulations as 0.926/0.074 agrees remarkably well
424 with HS-AFM observations of 0.925/0.075.
425 Although the simplified mechanical model of ATP-free M5 translocation does not resolve the
426 detailed physical processes underlying an M5 step upon mechanical T-head detachment (and
427 therefore does not allow us to infer their corresponding energetics), the numerical investigations
428 confirm the HS-AFM observations that the process of rebinding and strain generation in the L-
429 head does not require the execution of ATP-related conformational changes (i.e., the recovery
430 stroke and the powerstroke) and corresponding chemical energy input.

431 **MD-separations after ATP-free and ATP-dependent forward steps**

432 Although the MD-separation formed after forward stepping is not directly related to the main
433 subject of this study (i.e., the energy conversion mechanism), two observed results and their
434 interpretations are briefly described here. The first result is that two MD-separations of $N_{m\text{-}m}$ = 13
435 and 15 showed similar landing rates in the ATP-free walking (10.4 s^{-1} for $N_{m\text{-}m}$ =13 and 10.9 s^{-1} for

436 $N_{m\text{-}m}$ = 15; Fig. 4f,g). The number of events with $N_{m\text{-}m}$ = 11 was too small to be analysed. The
437 landing rate is influenced by the energy required for the thermal recovery stroke, $1/2\, k'\Delta\varphi_{rs}^2$, and
438 the energy required for the forward orientation of the bound head $U_D(\varphi_L)$, the sum of which is not
439 significantly different between the two MD-separations: 6.87 k_BT for $N_{m\text{-}m}$ = 13 ($\Delta\varphi_{rs}$ = 85˚ and φ_L
440 = 45˚) and 7.83 k_BT for $N_{m\text{-}m}$ = 15 ($\Delta\varphi_{rs}$ = 95˚ and φ_L = 35˚). This small difference, ~1 k_BT, is roughly
441 consistent with the small difference in the landing rate, considering the insufficient time resolution
442 of HS-AFM imaging, as well as the limited number of stepping events with $N_{m\text{-}m}$ = 15.

443 The second result is the distribution of MD-separations taken immediately after forward
444 stepping in ATP-free and ATP-dependent walking (Supplementary Fig. 8). The MD-separation is
445 largely determined by the periodicity of F-actin that guides the positions of the L and T heads[36].
446 However, a discernible tendency is evident in the distributions across the three nucleotide
447 conditions, albeit small differences. That is, the probability of taking a step with a MD-separation
448 of $N_{m\text{-}m}$ = 15 is greater in the presence of ATP than in the presence of ADP. Additionally, the
449 probability of having $N_{m\text{-}m}$ = 15 is marginally lower at 0.1 μM ATP than at 1 μM ATP. These
450 tendencies cannot be explained by the energetics of M5. The helical pitch of F-actin remains
451 virtually unchanged during the Brownian search by the detached head, as judged from the foot
452 sliding rate (Table 2) that reflects the frequency of changes in the helical pitch of F-actin. Therefore,
453 even when taking the MD-separation of $N_{m\text{-}m}$ = 15 is energetically unfavourable, M5 always binds
454 to the corresponding actin site. One possibility that explains these nucleotide-dependent
455 tendencies is that the structure of phalloidin-bound F-actin may be susceptible to modulation by
456 nucleotides in solution, in an unknown mechanism. This possibility is suggested by the nucleotide
457 dependence of the foot sliding rate (Table 2).

458

459

460 **Table 2** | Foot sliding events observed under three nucleotide conditions

Nucleotide conditions	Total number of images	Number of foot sliding events	Imaging rate (fps)	Foot sliding rate (s^{-1})
1 mM ADP	25,790	287	3.0	0.033
0.1 µM ATP	7,441	135	6.67	0.12
1 µM ATP	5,709	175	6.67	0.20

461

462 ## Discussion

463 Before discussing the energy conversion mechanism in M5 walking, it is important to recapitulate
464 the recent debate on the timing of Pi release in myosins[28-34,36,59]. The debate is now being settled,
465 to which the crystal structure of myosin VI has contributed greatly[29]. This structure shows the
466 presence of Pi in the backdoor tunnel[35], not in the active site, while the lever-arm is in the pre-
467 powerstroke state[29,36,59]. Therefore, this structure suggests the possibility that the powerstroke
468 occurs when Pi is still somewhere near the tunnel exit or at the tunnel exit, thereby explaining the
469 observations of ~2-times slower release of Pi into solution than the lever-arm swing[31-33]. A
470 structural comparison between the primed pre-powerstroke state and the post-powerstroke state,
471 as revealed by time-resolved cryo-EM, also supports this view[23]. It is hard to believe that a large
472 force can be generated in weakly bound myosin head with ADP·Pi at the active site, without any
473 chemical transition. We therefore adopt the most plausible view that the force generation occurs
474 at some time after Pi has left from the active site but before it is released into solution. However,
475 even in this view, we will simply describe the force generation as occurring after Pi release.

476 Despite numerous single-molecule studies of M5 motility using optical methods[9-
477 12,15,17,18,20,25,47.48,50-53], the ATP energy conversion in M5 walking has been little studied. The energy
478 conversion mechanism in M5 is derived from the prevailing view developed from extensive studies
479 of the muscle actomyosin system[1,2,27,36,60]. Changes in the ATP free energy along the muscle
480 actomyosin ATPase reaction pathway have been estimated from measurements of ATPase
481 kinetics and thermodynamics[61,62]. In this system, the free energy changes occur primarily at the

482 stages of ATP binding-induced head dissociation[19], ATP hydrolysis to ADP·Pi accompanied by a
483 recovery stroke[20-22], Pi release accompanied by the change from weak to strong head binding to
484 actin[29,36], and ADP release[17,37]. The amounts of released energy in these stages are approximately
485 10, 2, 12, and 3 k_BT, respectively[61] (see Fig. 5a). This profile of free energy changes is likely to be
486 similar in the M5−actin system, although the free energy changes at the first (ATP binding), fourth
487 (Pi release), and last (ADP release) stages depend on the concentrations of free ATP, Pi, and ADP,
488 respectively. Indeed, the actin-activated hydrolysis of ATP to ADP·Pi by M5 is associated with a
489 free energy change of −2.3 k_BT[16], similar to the case of muscle myosin. As contractile force is
490 generated when muscle myosin is in the strongly bound state formed during or after Pi release, it
491 is rational to assume that the 12 kBT of free energy provided at the stage of Pi release is used to
492 rotate or strain the crossbridge at the converter hinge[1,2,27]; when this idea is applied to M5, this
493 process may be delineated as winding up a spiral spring at the converter hinge of the L-head (Fig.
494 5b), as structurally suggested recently[23]. It has therefore generally been thought that the chemical
495 energy of ATP is the source of the mechanical work (or strain energy) produced by the power
496 stroke. However, this energy conversion mechanism cannot account for the ATP-free walking
497 observed in this study.

498 In this study, we have presented two main lines of data supporting our view that the strong
499 binding energy between actin and ADP-bound M5 is converted into mechanical work during ATP-
500 dependent walking (Fig. 5c). Note that in our assay system, a load is applied against the walking
501 of M5 from the substrate surface. The first line of data shows that the strain energy accumulated
502 in the L-head, $U_{LCH}(\varphi_L) + U_{neck}[h(\varphi_L)]$, is almost identical between ATP-free and ATP-dependent
503 walking for the respective cases of MD-separations (Fig. 3e & Supplementary Fig. 6e,f). It is
504 difficult to understand this good quantitative agreement of strain energy if the mechanism of strain
505 energy generation and hence the mechanism of energy conversion into mechanical work differed
506 significantly between ATP-free and ATP-dependent walking. Therefore, this good agreement

strongly suggests that during the ATP-dependent walking of M5, the chemical free energy of ATP is not converted into the strain energy of ~10 k_BT and is therefore not converted into mechanical work. This view may not be far from the traditional view that muscle contractile tension is generated when actin−myosin binding is strengthened by the release of Pi, which is accompanied by the release of free energy by 12 k_BT. It is impossible (at least very difficult) to decompose this released energy into its individual components, such as the free energy changes caused by the Pi release itself, by binding between actin and ADP-bound head, and by conformational changes in myosin and actin. However, a significant fraction of the released free energy must originate from the strong head−actin binding energy.

The second line of supporting data is the foot stomping (brief head detachment) that occurs predominantly at the L-head in all the nucleotide conditions tested. This spontaneous brief detachment can be understood as being caused by the reduction in head-actin binding energy. The foot stomp rate was found to be comparable, irrespective of the different nucleotide conditions tested, thereby indicating a comparable level of reduction in head-actin binding energy, corresponding to the strain energy of ~10 k_BT. In addition to the two lines of data mentioned above, the energetic analysis and the computational simulations of ATP-free walking could quantitatively explain the success/failure ratio for the forward step of M5 caused by mechanical detachment of the T-head. Our proposition that the L-head−actin binding energy serves as the energy source for mechanical work appears to imply that the magnitude of the force generated by a single M5 molecule in the presence of ATP depends on the ionic strength; the force becomes greater as the ionic strength is reduced. However, the molecular strain of M5 in the DHB state does not seem sensitive to the ionic strength, as far as the L-head−actin binding is strong enough. In muscle, it is well known that the isometric tension increases as ionic strength decreases[e.g. 63,64]. However, interpreting this increased force in muscle is not straightforward. Single-molecule force measurements are ideal for addressing this issue. To the best of our knowledge, however,

532 systematic measurements of the force generated by a single myosin molecule have not been
533 performed at different ionic strengths.

534 Our view that M5 does not convert ATP chemical energy into mechanical work does not mean
535 that this chemical energy is not essential for the forward translocation. To use the strain energy
536 generated by L-head−actin binding for forward translocation, the strong association between the
537 T-head and actin must be broken[19]. ATP binding to the T-head breaks this strong bond, releasing
538 free energy of approximately 10 kBT, assuming that it is approximately the same between muscle
539 myosin and M5. Although it is very difficult to decompose this released free energy into constituent
540 components, the large binding energy between the NF T-head and ATP must be used to break the
541 T-head−actin bond. The binding energy between the NF T-head and actin is approximately 23.8
542 $k_B T$, corresponding to the equilibrium constant of 4.9×10^{-11} M (Ref. 16). Although the affinity of
543 the NF head for ATP is too high to measure experimentally, the ATP binding energy must be
544 comparable to 23.8 $k_B T$. In addition, the hydrolysis of ATP to ADP·Pi associated with a recovery
545 stroke[20-22] and a free energy change of −2.3 $k_B T$ (Ref. 16) plays an important role in increasing
546 the efficiency of the forward landing of the detached head as well as in preventing its backward
547 return. Thus, the major role of ATP chemical energy is to release the strain energy acquired by the
548 strong L-head−actin binding for the forward movement of M5. In addition, it lowers the energy
549 barrier for the forward step and raises the energy barrier for the backward return, thereby ensuring
550 the unidirectional process of M5 walking.

551 It is well known in various contexts that a protein can change its affinity for ligands, membranes,
552 or partner proteins when subjected to external mechanical stress[e.g.,65-67]. However, it has only
553 rarely been reported that a homo-oligomeric protein changes its binding affinity for a target as a
554 result of the structural strain caused by the multivalent binding. For example, double-headed IgGs
555 were observed to migrate non-unidirectionally on a two-dimensional antigen lattice, when the
556 adjacent epitopes were appropriately separated, whereas single-headed IgGs stably remained at

557 one antigenic site[68]. There are many homo-oligomeric proteins with structural symmetry that can
558 bind to a target with multiple binding sites[69]. Although not yet explored, these oligomeric proteins
559 may universally exploit the affinity reduction caused by strain generation due to multivalent binding.
560 M5 may be a special case where the strain energy gained in this way is used for unidirectional
561 movement and mechanical work. This energy conversion mechanism will be found in other motor
562 proteins and used for the potential creation of novel molecular motors.
563

564 # Methods

565 **Sample preparation**

566 The full length of M5 was prepared from chick brain[70] and digested with proteinase K in the
567 absence of Ca^{2+} to produce M5-HMM[39,41]. Instead of using an actin-copelleting method to purify
568 M5-HMM[39,41], we used a protein concentrator (Vivaspin 500 of 100,000 MWCO; Sartorius) and
569 washing buffer containing 20 mM imidazole-HCl (pH 7.6), 100 mM KCl, 2 mM $MgCl_2$, 1 mM EGTA,
570 5 mM DTT and 0.1 mM PMSF. This was because the short coiled-coil tail of M5-HMM occasionally
571 unfolds when it is bound to actin filaments in the absence of ATP[38,39]. Partially biotinylated (20%)
572 actin filaments from rabbit skeletal muscles were prepared and then stabilized with phalloidin[10].
573 Streptavidin, glucose, hexokinase and nucleotides were purchased from Wako Pure Chemicals,
574 and phalloidin was purchased from Sigma Aldrich. The synthetic lipids, 1,2-dipalmitoyl-sn-glycero-
575 3-phosphocholine (DPPC), positively charged 1,2-dipalmitoyl-3-trimethylammonium-propane
576 (DPTAP), and 1,2-dipalmitoyl-sn-glycero-3-phosphoethanolamine-N-(cap biotinyl) (biotin-cap-
577 DPPE), were purchased from Avanti Polar Lipids.

578 **HS-AFM observations**

579 A mica disc (1 mm in diameter) was glued onto the top of a sample stage (glass rod of 2 mm in
580 diameter and 2 mm in height) and its top surface was cleaved using Scotch tape. The mica-

581 supported lipid bilayers as a substrate surface were formed by the deposition of liposomes
582 prepared using DPPC, DPTAP and biotin-cap-DPPE (with a typical weight ratio of 0.85:0.05:0.1)
583 onto the freshly cleaved mica surface[38,71]. After rinsing the lipid bilayer substrate with buffer A (20
584 mM imidazole-HCl (pH 7.6), 25 mM KCl, 2 mM $MgCl_2$, 1 mM EGTA, 5 mM DTT), a drop (2 μl) of
585 streptavidin in buffer A (10 nM) was deposited on the surface for 3 min. After rinsing with buffer A,
586 a drop (2 μl) of partially biotinylated actin filaments (1 μM) in buffer A was deposited on the
587 substrate surface for 10 min. After rinsing with a solution containing 1 mM ADP (1 U ml^{-1}
588 hexokinase and 10 mM glucose were added to remove contaminating ATP) in buffer A, we
589 deposited a drop (2 μl) of the same solution plus M5-HMM (0.1 to 1 nM) on the substrate surface
590 and allowed it to sit for 3 min. Finally, the sample stage was mounted onto the scanning stage of
591 our HS-AFM apparatus[72,73] (to which the interactive mode was newly implemented) and immersed
592 in a cell chamber filled with the same solution (60 μl) without M5-HMM. All HS-AFM imaging
593 experiments were performed at room temperature (25˚C) in amplitude modulation mode. For the
594 usual imaging (no sample manipulation by the AFM tip) of the M5-HMM interacting with actin, the
595 cantilever free oscillation amplitude A_0 was set to 1.5 nm, while the set point amplitude during
596 imaging A_s was set to 0.85 × A_0 (= 1.28 nm). The mean oscillation energy loss per tip–sample
597 contact, ΔE_{ts}, was estimated to be $\Delta E_{ts} = \gamma k_c(A_0^2 - A_s^2)/(2Q_c)$ = 3.1–4.7 $k_B T$ (k_B, Boltzmann
598 constant; T = 298 in kelvin), where γ (≈ 0.9) is a correction factor that accounts for the amplitude
599 reduction caused by a cantilever resonant frequency shift toward a higher frequency by repulsive
600 tip–sample interactions, and k_c = 0.1–0.15 N/m and Q_c = 1.5 are the spring constant and the quality
601 factor of the short cantilevers used. For interactive mode imaging, the set point amplitude A_p was
602 typically set to 0.33 × A_0 (= 0.5 nm) to apply a strong force to a few closely adjacent positions on
603 either head of the actin-bound M5-HMM. Short cantilevers (BL-AC7DS-KU4; 7−8 μm long, 2 μm
604 wide and 90 nm thick) were custom-made by Olympus, whose resonant frequency, spring constant
605 and quality factor were f_c = 0.8−1.2 MHz in water. The spring constant of each cantilever was

606 estimated from its measured frequency spectrum of thermal oscillation in buffer A. The interactive
607 mode is described in Supplementary Fig. 1.

608 **Caged-ATP experiments**

609 For caged-ATP experiments combined with iHS-AFM observations, we installed the following
610 optical components in our HS-AFM system (Supplementary Fig. 5a,b): a UV-LED system of 365
611 nm (L11922-401 and C11924-111, Hamamatsu photonics, Japan) and a dichroic mirror that
612 reflects UV light (320–360 nm) and transmits visible light (500–700 nm). Continuous UV light was
613 irradiated onto a sample area around the cantilever through the same objective lens (ELDW 20XC,
614 Nikon, Japan) used for cantilever deflection detection. The power of the incident UV light at the
615 exit of the objective lens was 19 mW at 350 nm. The diameter of the focal region measured by the
616 half-intensity diameter was approximately 300 μm (Supplementary Fig. 5c), from which the focal
617 volume was estimated to be ~14 nL. As the volume of the liquid cell was 60 μL, the caged-ATP
618 experiments could be repeated many times. After M5-HMM was deposited onto a mica-supported
619 lipid bilayer surface containing immobilized actin filaments, the sample stage was rinsed with a
620 solution containing 20 μM caged-ATP, 1 U ml^{-1} hexokinase, and 10 mM glucose dissolved in buffer
621 A. Therefore, the ATP released from caged-ATP was quickly converted to ADP. Finally, the sample
622 stage was immersed in a cell chamber filled with the same solution (60 μl) without M5-HMM.
623 Before performing iHS-AFM observations, photolysis of caged-ATP was performed several times
624 to confirm whether M5 moved unidirectionally by photolysis of caged-ATP. This experiment
625 generated some ADP in solution, and therefore, the M5 molecules in the observation area were
626 presumably bound to ADP before the subsequent iHS-AFM imaging. Then, ATP-free walking was
627 observed for several steps, immediately after which caged-ATP was photolyzed while HS-AFM
628 images were captured continuously (Supplementary Fig. 5d; Supplementary Video 3).

629 **Mechanical properties of converter hinge in actin-bound single-headed M5**

630 The potential energy $U(\varphi)$ of the converter hinge determines the equilibrium distribution $P(\varphi) \propto$
631 $\exp(-U(\varphi)/k_B T)$ of the lever-arm angle φ relative to the orientation of F-actin measured from the
632 plus end side (Fig. 3a, inset). By fitting to the HS-AFM data of single-headed M5 bound to actin
633 observed in 1 mM ADP and NF conditions[38], we found that in both conditions, $U(\varphi)$ fits well to the
634 functional form of $U(\varphi) = [(bk_0 + k_1(\varphi - \varphi_0))/(b + (\varphi - \varphi_0))](1 - \cos(\varphi - \varphi_0))$ (Fig. 3b, black
635 lines). Here, φ_0 is the equilibrium angle: 28.5˚ at 1 mM ADP and 32.9˚ in the NF condition. The
636 other parameters are b = 34.4˚, k_0 = 23 k_BT and k_1 = 2.3 k_BT at 1 mM ADP, and b = 75.0˚, k_0 = 37.9
637 k_BT and k_1 = 4.1 k_BT in the NF condition. The stiffness of the converter hinge in 1 mM ADP and
638 NF conditions, i.e., the angular spring constants, $K_D(\varphi)$ and $K_{NF}(\varphi)$, were determined from $U(\varphi) =$
639 $(1/2)\, K(\varphi) \cdot (\varphi - \varphi_0)^2$ (Fig. 3b, red lines). The magnitude of the force $F(\varphi)$ in the direction parallel
640 -to F-actin generated at the free end of the lever-arm was obtained as $F(\varphi) = K(\varphi) \cdot$
641 $(\varphi - \varphi_0)^2/[L_{\mathrm{neck}}(cos\varphi_0 - cos\varphi)]/0.243$ (Fig. 3b, blue lines), where L_{neck} is the neck length (~23
642 nm estimated from nsEM images[42]) and the division by 0.243 is for unit conversion from k_BT to
643 pN·nm.

644 **Strain energy of M5 in DHB state**

645 To estimate the strain energy accumulated in a M5 molecule in the DHB state, we first measured
646 the following three geometrical parameters from HS-AFM images (Fig. 3c, inset): the tangential
647 angle of the L-head's neck region emerging from the motor domain, φ_L; the angle of the T-head
648 neck as a function of φ_L, $\varphi_T(\varphi_L)$; the deflection of the neck end of the L-head as a function of φ_L,
649 $h(\varphi_L)$. The angles, φ_L and φ_T, relative to the orientation of F-actin, were measured from the plus
650 end side of F-actin. The results are shown in Fig. 3c,d (for $N_{m\text{-}m}$ = 13 actin subunits),
651 Supplementary Fig. 6a,c (for $N_{m\text{-}m}$ = 11 actin subunits), and Supplementary Fig. 6b,d (for $N_{m\text{-}m}$ =
652 15 actin subunits). The total strain energy E_{total} is expressed as $E_{total} = U_D(\varphi_L) + U_X[\varphi_T(\varphi_L)] +$
653 $U_{neck}[h(\varphi_L)]$, where $U_D(\varphi_L)$ is the strain energy of the L-head converter hinge (the subscription D

denotes the ADP-bound state), $U_X[\varphi_T(\varphi_L)]$ is the strain energy of the T-head converter hinge (the subscription X is either D or NF depending on the nucleotide state of the T-head), and $U_{neck}[h(\varphi_L)]$ is the bending energy of the L-head's neck region. The DHB states formed during ATP-free and ATP-dependent walking are almost stationary, meaning that all forces acting on a M5 molecule, including constraining forces, are balanced. From the principle of 'virtual work' in mechanics, the work done by the non-constraining forces (i.e., the forces generated by the two converter hinges and the bending of the L-head) is zero, which can be expressed as

$$\left[\frac{\partial U_{\mathrm{D}}(\varphi_{\mathrm{L}})}{\partial \varphi_{\mathrm{L}}} + \frac{\partial U_{\mathrm{X}}[\varphi_{\mathrm{T}}(\varphi_{\mathrm{L}})]}{\partial \varphi_{\mathrm{T}}}\frac{\partial \varphi_{\mathrm{T}}}{\partial \varphi_{\mathrm{L}}} + \frac{\partial U_{\mathrm{neck}}[h(\varphi_{\mathrm{L}})]}{\partial h}\frac{\partial h}{\partial \varphi_{\mathrm{L}}}\right] \cdot \delta\varphi_{\mathrm{L}} = 0, \qquad (1)$$

where $\delta\varphi_{\mathrm{L}}$ is the virtual displacement. Therefore, the total strain energy E_{total} is conserved. The results obtained for E_{total}, $U_D(\varphi_L) + U_X[\varphi_T(\varphi_L)]$, $U_{neck}[h(\varphi_L)]$, $U_X[\varphi_T(\varphi_L)]$, and the spring constant of the L-head neck k_{neck} are shown in Fig.3e,f for $N_{m\text{-}m} = 13$, Supplementary Fig.6e,g for $N_{m\text{-}m} = 11$, and Supplementary Fig.6f,h for $N_{m\text{-}m} = 15$.

Mechanical model and simulations

To obtain relevant numerical estimates for ATP-free stepping from mathematical modelling, a simple representation of the M5 dimer was employed, with the shape (in the characteristic HS-AFM planar geometry) characterized by only three variables: the angles ϕ_1 and ϕ_2 for the two neck–motor domain junctions and the neck–neck junction angle ϕ_c (Supplementary Fig. 9). To simplify the simulations, our energy does not include a contribution due to elastic bending of the necks (i.e., $h = 0$). Instead, this elastic energy was included to the energy of L-head converter hinge. The neck–motor domain junction angle ϕ used in the M5 model and the maximum lever-arm angle $\varphi_L^{max} = 135^\circ$ are related via $\phi - \phi_0 = \varphi_L^{max} - \varphi_0$, where the equilibrium angle $\phi_0 = 148.5^\circ$ of the neck–motor domain junction corresponds to the equilibrium lever-arm angle $\varphi_0 = 28.5^\circ$ relative to the actin filament (see Supplementary Methods).

The total energy of DHB M5 is $E = U(\phi_1) + U(\phi_2) - 2\epsilon$, where ϵ is the absolute value of the actin-binding energy of the M5 head. As done for previous models[54,55], we assumed that the neck–neck junction was highly flexible and that there was no contribution to the elastic energy coming from it.

Conformational motions that underlie M5 stepping proceed on the timescales of milliseconds, where inertial effects are negligible, and only overdamped motions with velocities instantaneously following the applied forces occur. Therefore, the stochastic Langevin description, which effectively accounts for the interactions of M5 with the surrounding environment via viscous friction, is applicable. To numerically investigate ATP-free M5 translocation, Brownian dynamics simulations were performed for the five beads representing the rigid rods in our mechanical model (Supplementary Figs. 9,10). The dynamic evolution of the M5 five-bead model is therefore described by equations for the beads $\frac{d}{dt}\vec{R}_i = -\frac{\partial E}{\partial \vec{R}_i} + \sqrt{2\Theta}\vec{\xi}_i(t)$, $E = U(\phi_1) + U(\phi_2) + \sum_{i=1}^{4} \frac{1}{2}\kappa_s(\Delta l_i)^2$, and $< \xi_{i,\alpha}(t)\xi_{j,\beta}(t) >= \delta_{ij}\delta_{\alpha\beta}\delta(t)$. Here, $\vec{R}_i = (X_i, Y_i)^T$ is the instantaneous position of bead i. In the reduced equations, lengths were measured in units of the neck length $l_n = 36/\sqrt{2}$ nm, and time was measured in units of $\mu l_n^2/k_0$, where μ is the viscous friction coefficient of beads and $k_0 = 23\ k_B T$. Hence, converter hinge energies $U(\phi)$ were measured in units of k_0. The total potential energy E of the 5-bead model is the sum of both converter hinge energies. The expression of E contains additional barriers of dimensionless strength $\kappa_s = 150$, which prevent length changes Δl of the motor domains and neck rods ($\Delta l_i = \left|\vec{R}_{i+1} - \vec{R}_i\right| - l_i^{(0)}$). The dimensionless quantity Θ, which determines the fluctuation intensity of beads, was related to the equilibrium converter hinge stiffness k_0 , i.e., $\Theta = k_B T/k_0 = 1/23$. Starting from the configuration with both myosin heads bound to the actin filament, the set of equations was numerically integrated to obtain bead positions $\vec{R}_i = (X_i, Y_i)^T$ at any time moment. In the simulations, the Euler scheme with a dimensionless time-step of $5 \cdot 10^{-4}$ was employed. In our

dimensionless numerical model, time was measured in units of $\tau = \mu l_n^2/k_0$. Introducing the bead mobility $\Gamma = 1/\mu$ and using the dimensionless quantity $\Theta = k_B T/k_0$, we obtain $\tau = \frac{\Theta l_n^2}{\Gamma k_B T}$. Using the Einstein relation $\Gamma k_B T = D$, it is expressed as $\tau = \Theta l_n^2/D$. Assuming a diffusion constant of $D = 10^{-7}\mathrm{cm}^2/\mathrm{s}$, we obtain a time unit of approximately $\tau = 3\ \mu s$. This estimate was applied to relate timescales of model simulations to observations from HS-AFM experiments. Consistent with the approximate character of the model, the actin filament and interactions of M5 heads with it were accounted for in a simplified way. For details of the model, its parameters, and numerical simulations, refer to the Supplementary Fig. 9, Supplementary Table 1, and Supplementary Methods.

Data availability

Data supporting the findings of this study are included within the article and supplementary figures. The videos analysed to generate Fig. 3c-f are partially included as Supplementary Videos 1 and 2 (because many video images were used for Fig.3c-f, we will provide them upon request). It is also the same for the videos analysed for Tables 1 and 2. Source data for Fig.3a,c,d, Fig. 4d-g, Supplementary Fig,6,a-d, and Supplementary Fig.10l are provided with this paper.

Code availability

This study does not produce code applicable for other purposes.

References

1. Geeves, M. A. The ATPase mechanism of myosin and actomyosin. *Biopolymers* **105**, 483–491 (2016).
2. Vale, R. D. & Milligan, R. A. The way things move: Looking under the hood of molecular motor proteins. *Science* **288**, 88–95 (2000).
3. Cross, R. A. Mechanochemistry of the kinesin-1 ATPase. *Biopolymers* **105**, 476–482 (2016).
4. Schmidt, H. & Carter, A. P. Structure and mechanism of the dynein motor ATPase. *Biopolymers* **105**, 557–567 (2016).
5. Adachi, K. et al. Coupling of rotation and catalysis in F_1-ATPase revealed by single-molecule imaging and manipulation. *Cell* **130**, 309–321 (2007).
6. Hwang, W. & Karplus, M. Structural basis for power stroke vs. Brownian ratchet mechanisms of motor proteins. *Proc. Natl. Acad. Sci. U. S. A*. **116**, 19777–19785 (2019).
7. Howard, J. Motor proteins as nanomachines: The roles of thermal fluctuations in generating force and motion. *Biol. Phys*. **60**, 47–59 (2011).
8. Howard, J. Protein power strokes. *Curr. Biol*. **16**, R517–R519 (2006).
9. Mehta, A. D., Rock, R. S., Rief, M., Spudich, J. A., Mooseker, M. S. & Cheney, R. E. *Nature* **400**, 590–593 (1999).
10. Sakamoto, T., Amitani, I., Yokota, E. & Ando, T. Direct observation of processive movement by individual myosin V molecules. *Biochem. Biophys. Res. Commun*. **272**, 586–590 (2000).
11. Yildiz, A. *et al*. Myosin V walks hand-over-hand: single fluorophore imaging with 1.5-nm localization. *Science* **300**, 2061–2065 (2003).
12. Sakamoto, T., Webb, M. R., Forgacs, E., White, H. D. & Sellers, J. R. Direct observation of the mechanochemical coupling in myosin Va during processive movement. *Nature* **455**, 128–132 (2008).

749 13. Rosenfeld, S. S. & Sweeney, H. L. A model of myosin V processivity. *J. Biol. Chem*. 279,
750 40100–40111 (2004).
751 14. Walker, M. L., Burgess, S. A., Sellers, J. R., Wang, F., Hammer III, J. A., Trinick, J. & Knight,
752 P. J. Two-headed binding of a processive myosin to F-actin. *Nature* **405**, 804–807 (2000).
753 15. Oguchi, Y., Mikhailenko, S. V., Ohki, T., Olivares, A. O., De La Cruz, E. M. & Ishiwata, S. Load-
754 dependent ADP binding to myosins V and VI: Implications for subunit coordination and function.
755 *Proc. Natl. Acad. Sci. U. S. A.* **105**, 7714–7719 (2008).
756 16. De La Cruz, E. M., Wells, A. L., Rosenfeld, S. S., Ostap, E. M. & Sweeney, H. L. The kinetic
757 mechanism of myosin V. *Proc. Natl. Acad. Sci. U. S. A.* **96**, 13726–13731 (1999).
758 17. Veigel, C., Schmitz, S., Wang, F. & Sellers, J. R. Load-dependent kinetics of myosin-V can
759 explain its high processivity. *Nat. Cell Biol*. **7**, 861–869 (2005).
760 18. Purcell, T. J., Sweeney, H. L. & Spudich, J. A. A force-dependent state controls the coordination
761 of processive myosin V. *Proc. Natl. Acad. Sci. U. S. A*. **102**, 13873–13878 (2005).
762 19. Coureux, P.-D., Wells, A. L., Ménétrey, J., Yengo, C. M., Morris, C. A., Sweeney, H. L. &
763 Houdusse, A. Structural state of the myosin V motor without bound nucleotide. *Nature* **425**,
764 419–423 (2003).
765 20. Shiroguchi, K., Chin, H. F., Hannemann, D. E., Muneyuki, E., De La Cruz, E. M. & Kinosita Jr.
766 K. Direct observation of the myosin Va recovery stroke that contributes to unidirectional
767 stepping along actin. *PLoS. Biol.* **9**, e1001031 (2011).
768 21. Coureux, P.-D., Sweeney, H. L. & Houdusse, A. Three myosin V structures delineate essential
769 features of chemo-mechanical transduction. *EMBO J*. **23**, 4527–4537 (2004).
770 22. Fischer, S., Windshügel, B., Horak, D., Holmes, K. C. & Smith, J. C. Structural mechanism of
771 the recovery stroke in the myosin molecular motor. *Proc. Natl. Acad. Sci. U. S. A*. **102**, 6873–
772 6878 (2005).

773 23. Klebl, D. P. et al. Swinging lever mechanism of myosin directly shown by time-resolved cryo-
774 EM. *Nature* **642**, 519–526 (2025).
775 24. Fineberg, A. et al. Myosin-5 varies its step length to carry cargo straight along the irregular F-
776 actin track. *Proc. Natl. Acad. Sci. U. S. A.* **121**, e2401625121 (2024).
777 25. Ali, M. Y., Uemura, S., Adachi, K., Itoh, H., Kinosita Jr. K. & Ishiwata, S. Myosin V is a left-
778 handed spiral motor on the right-handed actin helix. *Nat. Struct. Biol.* **9**, 464-467 (2002).
779 26. Vale, R. D. Myosin V motor proteins: marching stepwise towards a mechanism. J. Cell Biol.
780 163, 445–450 (2003).
781 27. Spudich, J. A. The myosin swinging cross-bridge model. *Nat. Rev. Mol. Cell Biol*. **2**, 387–392
782 (2001).
783 28. Hwang, Y., Washio, T., Hisada, T., Higuchi, H. & Kaya, M. A reverse stroke characterizes the
784 force generation of cardiac myofilaments, leading to an understanding of heart function. *Proc.*
785 *Natl. Acad. Sci. U. S. A*. **118**, e2011659118 (2021).
786 29. Llinas, P. et al. How actin initiates the motor activity of myosin. *Dev. Cell* **33**, 401–412 (2015).
787 30. Stehle, R. Force responses and sarcomere dynamics of cardiac myofibrils induced by rapid
788 changes in [Pi]. *Biophys*. *J*. **112**, 356–367 (2017).
789 31. Trivedi, D. V., Muretta, J. M., Swenson, A. M., Davis, J. P., Thomas, D. D. & Yengo, C. M.
790 Direct measurements of the coordination of lever arm swing and the catalytic cycle in myosin
791 V. *Proc. Natl. Acad. Sci. U. S. A.* **112**, 14593–14598 (2015).
792 32. Muretta, J. M., Rohde, J. A., Johnsrud, D. O., Cornea, S. & Thomas, D. D. *Proc. Natl. Acad.*
793 *Sci. U. S. A.* **112**, 14272–14277 (2015).
794 33. Woody, M. S., Winkelmann, D. A., Capitanio, M., Ostap, E. M. & Goldman, Y. E. Single
795 molecule mechanics resolves the earliest events in force generation by cardiac myosin. *eLife*
796 **8**, e49266 (2019).

797 34. Caremani, M., Melli, L., Dolfi, M., Lombardi, V. & Linari, M. The working stroke of the myosin
798 II motor in muscle is not tightly coupled to release of orthophosphate from its active site. *J.*
799 *Physiol.* **591**, 5187–5205 (2013).
800 35. Yount, R, G., Lawson, D. & Rayment, I. Is myosin a "back door" enzyme? *Biophys. J.* **68**, 44s–
801 49s (1995).
802 36. Robert-Paganin, J., Pylypenko, O., Kikuti, C., Sweeney, H. L. & Houdusse, A. Force generation
803 by myosin motors: A structural perspective. *Chem. Rev*. **120**, 5−35 (2020).
804 37. Oke, O. A. et al. Influence of lever structure on myosin 5a walking. *Proc. Natl Acad. Sci. U. S.*
805 *A.* **107**, 2509–2514 (2010).
806 38. Kodera, N., Yamamoto, D., Ishikawa, R. & Ando, T. Video imaging of walking myosin V by
807 high-speed atomic force microscopy. *Nature* **468**, 72–76 (2010).
808 39. Wang, F., Chen, L., Arcucci, O., Harvey, E. V., Bowers, B., Xu, Y., Hammer III, J. A. & Sellers,
809 J. R. Effect of ADP and ionic strength on the kinetic and motile properties of recombinant
810 mouse myosin V. *J. Biol. Chem*. **275**, 4329–4335 (2000).
811 40. Espindola, F. S. et al. The light chain composition of chicken brain myosin-Va: Calmodulin,
812 myosin-II essential light chains, and 8-kDa dynein light chain/PIN. *Cell Motil. Cytoskel.* **47**,
813 269–281 (2000).
814 41. Koide, H. et al. Identification of the specific IQ motif of myosin V from which calmodulin
815 dissociates in the presence of Ca^{2+}. *Biochemistry* **45**, 11598–11604 (2006).
816 42. Burgess, S. et al. The prepower stroke conformation of myosin V. *J. Cell Biol*. **159**, 983–991
817 (2002).
818 43. Haruyama, T., Uchihashi, T., Yamada, Y., Kodera, N., Ando, T. & Konno, H. Negatively charged
819 lipids are essential for functional and structural switch of human 2-Cys peroxiredoxin II. *J. Mol.*
820 *Biol*. **430**, 602–610 (2018).

44. Owa, M. et al. Inner lumen proteins stabilize doublet microtubules in cilia and flagella. *Nat. Commun*. **10**, 1143 (2019).

45. Ando, T., Uchihashi, T. & Scheuring, S. Filming biomolecular processes by high-speed atomic force microscopy. *Chem. Rev.* **114**, 3120–3188 (2014).

46. Uchihashi, T., Iino, R., Ando, T. & Noji, H. High-speed atomic force microscopy reveals rotary catalysis of rotorless F1-ATPase. *Science* **333**, 755–758 (2011).

47. Uemura, S., Higuchi, H., Olivares, A. O., De La Cruz, E. M., Ishiwata, S. Mechanochemical coupling of two substeps in a single myosin V motor. *Nat. Struct. Mol. Biol*. **11**, 877–883 (2004).

48. Gebhardt, J. C. M., Clemen, A. E.-M., Jaud, J. & Rief, M. Myosin-V is a mechanical ratchet. *Proc. Natl. Acad. Sci. U. S. A*. **103**, 8680–8685 (2006).

49. Kad, N. M., Trybus, K. M. & Warshaw, D. M. Load and Pi control flux through the branched kinetic cycle of myosin V. *J. Biol. Chem*. **283**, 17477–17484 (2008).

50. Andrecka, J. et al. Structural dynamics of myosin 5 during processive motion revealed by interferometric scattering microscopy. *eLife* 4, e05413 (2015).

51. Beausang, J. F., Shroder, D. Y., Nelson, P. C. & Goldman Y. E. Tilting and wobble of myosin V by high-speed singlemolecule polarized fluorescence microscopy. *Biophys. J*. **104**, 1263–1273 (2013).

52. Dunn, A. R & Spudich, J. A. Dynamics of the unbound head during myosin V processive translocation. *Nat. Struct. Mol. Biol*. **14**. 246–248 (2007).

53. Fujita, K., Iwaki, M., Iwane, A. H., Marcucci, L. & Yanagida T. Switching of myosin-V motion between the lever-arm swing and Brownian search-and-catch. *Nat. Commun*. **3**, 956 (2012).

54. Hinczewski, M., Tehver, R. & Thirumalai, D. Design principles governing the motility of myosin V. *Proc. Natl. Acad. Sci. U. S. A*. **110**, E4059–E4068 (2013).

55. Craig, E. M. & Linke, H. Mechanochemical model for myosin V. *Proc. Natl. Acad. Sci. U. S. A*. **106**, 18261–18266 (2009).

846 56. Takagi, Y. et al. Myosin-10 produces its power-stroke in two phases and moves processively
847 along a single actin filament under low load. *Proc. Natl. Acad. Sci. U. S. A*. **111**, E1833–E1842
848 (2014).
849 57. Wulf, S. F. et al. Force-producing ADP state of myosin bound to actin. *Proc. Natl. Acad. Sci. U.*
850 *S. A*. **113**, E1844–E1852 (2016).
851 58. Billington, N., Revill, D. J., Burgess, S. A., Chantler, P. D. & Knight, P. J. Flexibility within the
852 heads of muscle myosin-2 molecules. *J. Mol. Biol*. **426**, 894–907 (2014).
853 59. Houdusse, A. & Sweeney, H. L. How myosin generates force on actin filaments. *TIBS* **41**, 989–
854 997 (2016).
855 60. Geeves, M. A. & Holmes, K. C. Structural mechanism of muscle contraction. *Annu. Rev.*
856 *Biochem*. **68**, 248 687–728 (1999).
857 61. Howard, J. *Mechanics of Motor Proteins and the Cytoskeleton*. Sinauer Associates, Inc.
858 Sunderland, Massachusetts (2001).
859 62. Kodama, T. Thermodynamic analysis of muscle ATPase mechanisms. *Physiol. Rev*. **65**, 467–
860 551 (1985).
861 63. Sugi, H. et al. Enhancement of force generated by Individual myosin heads in skinned rabbit
862 psoas muscle fibers at low ionic strength. *PLOS ONE* **8**, e63658 (2013).
863 64. Karatzaferi, C., Chinn, M. K. & Cooke, R. The force exerted by a muscle cross-bridge depends
864 directly on the strength of the actomyosin bond. *Biophys. J*. **87** 2532–2544 (2004).
865 65. Braun, A. R., Lacy, M. M., Ducas, V. C., Rhoades, E. & Sachs, J. N. α-synuclein-induced
866 membrane remodeling is driven by binding affinity, partition depth, and interleaflet order
867 asymmetry. *J. Am. Chem. Soc*. **136**, 9962−9972 (2014).
868 66. Jaalouk, D. E. & Lammerding, J. Mechanotransduction gone awry. *Nat. Rev. Mol. Cell Biol*. **10**,
869 63−73 (2009).

870 67. Xie, W. et al. Static and dynamic: Evolving biomaterial mechanical properties to control cellular
871 mechanotransduction. *Adv. Sci.* **10**, 2204594 (2023).
872 68. Preiner, J. et al. IgGs are made for walking on bacterial and viral surfaces. *Nat. Commun*. **5**,
873 4394 (2014).
874 69. Goodsell, D. S. & Olson, A. J. Structural symmetry and protein function. *Annu. Rev. Biophys.*
875 *Biomol. Struct*. **29**, 105–53 (2000).
876 70. Cheney, R. E. Purification and assay of myosin V. *Methods Enzymol.* **298**, 3–18 (1998).
877 71. Yamamoto, D. et al. High-speed atomic force microscopy techniques for observing dynamic
878 621 biomolecular processes. *Methods Enzymol*. **475**, 541–564 (2010).
879 72. Ando, T., Uchihashi, T. & Fukuma, T. High-speed atomic force microscopy for nano-
880 visualization of dynamic biomolecular processes. *Prog. Surf. Sci*. **83**, 337–437 (2008).
881 73. Ando, T. *High-Speed Atomic Force Microscopy in Biology*. Springer Berlin, Heidelberg (2022).
882

883 **Acknowledgements**

884 We thank A. Mikhailov for advising us about the modelling and simulations of ATP-free walking of
885 M5, and R. Vale and J. Howard for critical reading of the original manuscript. We acknowledge
886 Grant-in-Aid for Scientific Research (S) #24227005 and #17H06121 (T.A.), (A) #22H00405 (T.A.)
887 and (C) #21K03483 (H.F.) from the Japan Society for the Promotion of Science, the Human
888 Frontier Science Program grant #RGP0019 (T.A.), the PRESTO grant #JPMJPR13L4 (N.K.) from
889 the Japan Science and Technology Agency, and the Transdisciplinary Research Promotion grant
890 (H.F. and N.K.) from NanoLSI-WPI for financial support of this work.

891 **Author information**

892 Contributions

893 T.A. conceptualized this study and the iHS-AFM technique. N.K. constructed a UV-illumination
894 system and installed it to the HS-AFM system, performed all experiments and analysed the image

data. T.U. developed a software program for iHS-AFM. H.F. performed modelling and simulations of ATP-free M5 translocation. T.A. analysed the strain energy. H.F. and T.A. analysed the energetics of ATP-free and ATP-dependent M5 walking. T.A. wrote the manuscript and all authors provided feedback and editorial support.

Correspondence and requests for materials should be addressed to Toshio Ando

Ethics declarations

Competing interests

The authors declare no competing interests.

Additional Information

Supplementary Information

Description of Additional Supplementary Files

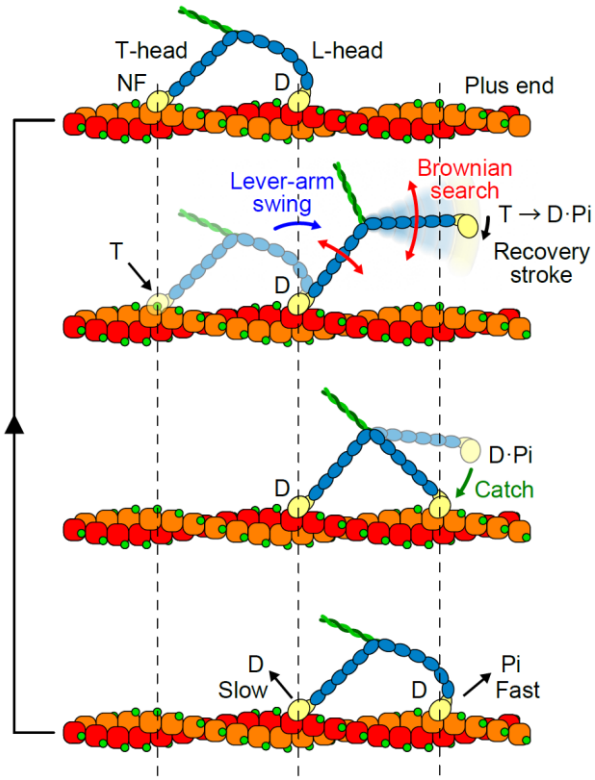

908 **Fig. 1 | Generally accepted chemomechanical cycle in walking M5.** NF, D, Pi, D·Pi, and T
909 denote nucleotide-free, ADP, inorganic phosphate, ADP·Pi, and ATP, respectively. See the main
910 text for details.
911

912

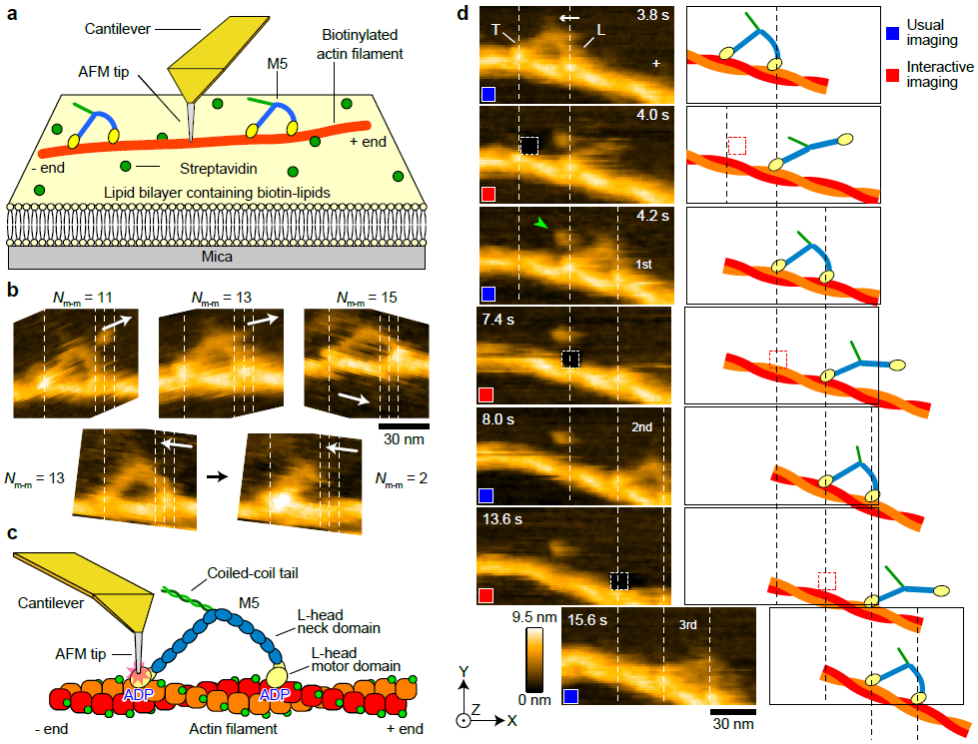

Fig. 2 | iHS-AFM imaging of ATP-free walking of M5. a Schematic of the assay system used for the imaging of ATP-free and ATP-dependent walking of M5 (see Methods). **b** Typical HS-AFM images showing actin-bound M5 with different MD-separations: top, in the presence of 1 mM ADP; bottom, in the presence of 1 μM ATP. The white arrows indicate the X-scanning directions during image acquisition. **c** Schematic showing the application of a strong tip force to an ADP-bound motor domain. **d** Typical successive HS-AFM images showing ATP-free walking of M5. Scan area, 130 × 65 nm^2; number of pixels, 80 × 40 pixels; frame rate, 5 fps. A strong force was applied to the areas (7 × 7 pixels; dark rectangles) encircled with a white dashed line (4.0, 7.4 and 13.6 s). White arrow, coiled-coil tail of M5 tilted toward the minus end of F-actin; vertical dashed lines, the centres of mass of the motor domains; plus sign, the plus end of F-actin. The schematics on the right-hand side explain the AFM images, where the areas to which strong force was applied are marked with red dashed lines. The images were acquired while the tip was being scanned towards the +X and +Y directions during raster scanning.

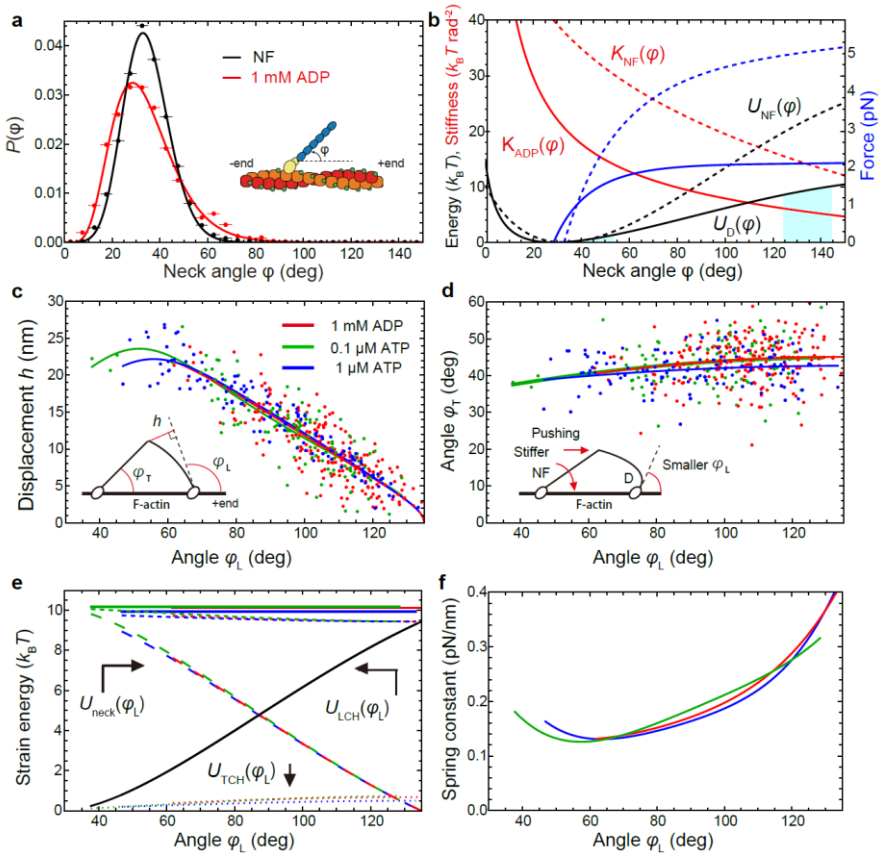

Fig. 3 | Mechanical properties of converter hinges and L-head neck of M5 in three nucleotide conditions. a Distributions of neck angle of actin-bound single-headed M5 in the NF and 1 mM ADP conditions. The horizontal bars indicate bin width 5˚. **b** Angle-dependence of stiffness (red) and energy (black) of converter hinge, and the magnitude of force in the direction of F-actin generated at the free end of the neck (blue). The solid and broken lines are those for 1 mM ADP and NF conditions, respectively. **c−f** Mechanical properties of M5 with MD-separation of $N_{m\text{-}m}$ = 13. The lines are drawn within the observed angle ranges of φ_L. The colour code shown in (**c**) is common in (**c−f**), except for the black line in (**e**). In (**c**), lever-arm displacement h depending on the angle φ_L is shown. The solid lines were obtained by fitting the plotted data to fourth polynomial functions. The inset shows three geometrical parameters (φ_L, φ_T, and h) measured. In(**d**), dependence of φ_T on φ_L is shown. The solid lines were obtained by fitting the plotted data to second polynomial functions. The inset shows the stiffer NF T-head pushing the neck−neck junction. In (**e**), strain energies as a function of φ_L are shown. U_{TCH} and U_{LCH} are strain energies of the converter hinges at the T and L heads, respectively. U_{neck} is the bending energy of the L-head neck. The top horizontal solid lines show the total strain energy (U_{TCH} + U_{LCH} + U_{neck}), and the dashed lines slightly below the horizontal solid lines show U_{LCH} + U_{neck}. In (**f**), spring constants of L-head neck bending, k_{neck}, are shown.

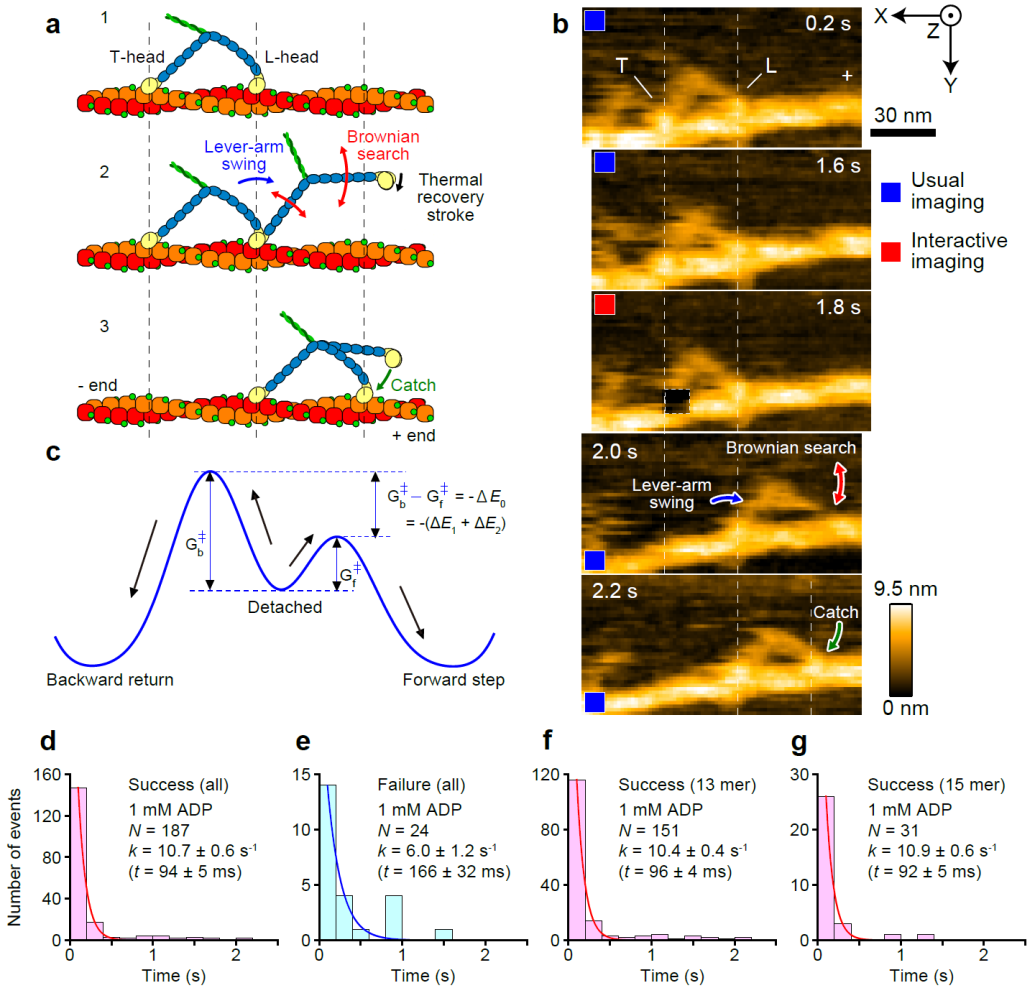

Fig. 4 | Transition events in ATP-free walking of M5. a Schematic showing transition events occurring between the T-head detachment and its final binding to a front actin site. **b** Energy landscape leading the detached head to forward step or backward return. Both the activation energies ($G_f^{\ddagger}$ and $G_b^{\ddagger}$) are assumed to contain an identical unspecifiable component in addition to E_1 (thermal recovery stroke energy only for the forward step) and E_2 (energy for lever-arm swing). **c** Typical successive HS-AFM images showing transition events. Scan area, 130 × 65 nm^2; number of pixels, 80 × 40; frame rate, 5 fps. A strong force was applied to the area (7 × 7 pixels; dark rectangle) encircled with a white dashed line (1.8 s). The images were acquired while the tip was being scanned towards the +X and +Y directions during raster scanning. **d-g** Histograms of time duration between T-head detachment by tip-force and its landing on a front actin site (**d,f,g**) or on an original actin site or its vicinity (**e**). The red and blue lines indicate a single exponential function fitted to the respective histograms. Note that the time resolution is limited to the image acquisition time (200 ms). In (**d,e**), all data are combined without distinguishing the MD-separations after landing. In (**f**), only data with $N_{m\text{-}m}$ = 13 are combined. In (**g**), only data with $N_{m\text{-}m}$ = 15 are combined.

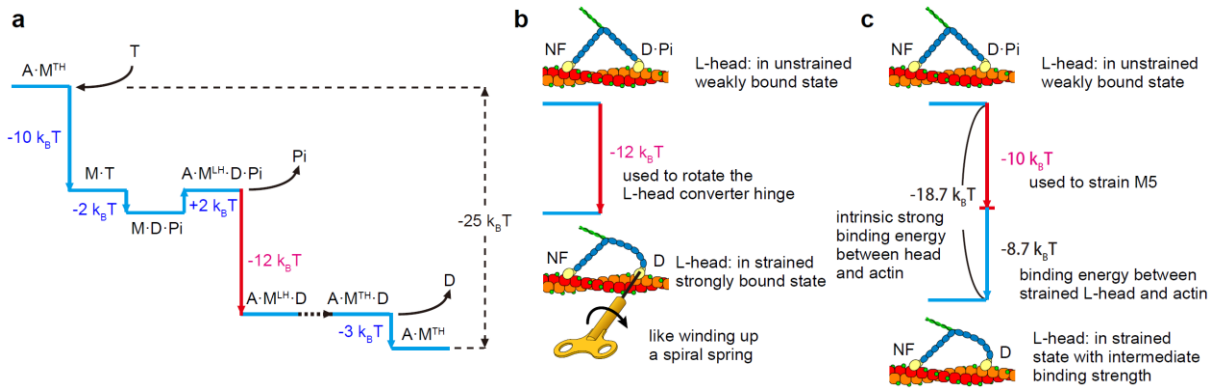

Fig. 5 | Mechanism of energy conversion into mechanical work in M5. A, M, T, D, Pi, and NF denote actin, M5, ATP, ADP, orthophosphate, and nucleotide-free, respectively. **a** Free energy changes along the ATPase reaction of M5−actin. Since some values of free energy changes are not yet available for M5−actin, the values shown correspond to those for skeletal actomyosin[61]. The superscripts, TH and LH, denote the trailing head and leading head, respectively. During the transition from $A{\cdot}M^{LH}{\cdot}D$ to $A{\cdot}M^{TH}{\cdot}D$ (black dotted line), the second head detaches from actin to become the new L-head. **b** Conventional mechanism of energy transduction to mechanical work. In this mechanism, the free energy ~12 k_BT released at the transition from $A{\cdot}M^{LH}{\cdot}D{\cdot}Pi$ to $A{\cdot}M^{LH}{\cdot}D$, shown with the red line in (**a**), is assumed to be used to actively rotate the lever-arm around the L-head converter hinge, like winding up a spiral spring. By this rotation, the L-head is strained. **c** New mechanism proposed in this study. More than 50% of the strong binding energy between actin and the ADP-bound L-head is used to strain the M5 molecule predominantly at the L-head. This results in weaker binding of the L-head to actin. Here, the binding energy between M·D·Pi and actin is assumed to be negligibly small, compared to that between M·D and actin.